

## Surface Effects on the Mott-Hubbard Transition in Archetypal $V_2O_3$

G. Lantz,<sup>1,\*</sup> M. Hajlaoui,<sup>1</sup> E. Papalazarou,<sup>1</sup> V. L. R. Jacques,<sup>1</sup> A. Mazzotti,<sup>1</sup> M. Marsi,<sup>1</sup> S. Lupi,<sup>2</sup>  
M. Amati,<sup>3</sup> L. Gregoratti,<sup>3</sup> L. Si,<sup>4</sup> Z. Zhong,<sup>4,5</sup> and K. Held<sup>4</sup>

<sup>1</sup>Laboratoire de Physique des Solides, CNRS-UMR 8502, Université Paris-Sud, F-91405 Orsay, France

<sup>2</sup>Dipartimento di Fisica, Università di Roma La Sapienza, Piazzale Aldo Moro, I-00185 Roma, Italy

<sup>3</sup>Elettra-Sincrotrone Trieste SCpA, SS 14 km 163.5 AREA Science Park, 34149 Basovizza, Trieste, Italy

<sup>4</sup>Institute for Solid State Physics, Vienna University of Technology, AT-1040 Vienna, Austria

<sup>5</sup>Institute for Theoretical and Astrophysics, University of Würzburg, Am Hubland, 9704 Würzburg, Germany

(Received 8 July 2015; revised manuscript received 7 October 2015; published 2 December 2015)

We present an experimental and theoretical study exploring surface effects on the evolution of the metal-insulator transition in the model Mott-Hubbard compound Cr-doped  $V_2O_3$ . We find a microscopic domain formation that is clearly affected by the surface crystallographic orientation. Using scanning photoelectron microscopy and x-ray diffraction, we find that surface defects act as nucleation centers for the formation of domains at the temperature-induced isostructural transition and favor the formation of microscopic metallic regions. A density-functional theory plus dynamical mean-field theory study of different surface terminations shows that the surface reconstruction with excess vanadyl cations leads to doped, and hence more metallic, surface states, which explains our experimental observations.

DOI: 10.1103/PhysRevLett.115.236802

PACS numbers: 71.30.+h, 73.20.At

Metal-to-insulator transitions (MITs) are among the most remarkable macroscopic effects of electronic correlations in condensed matter. After many experimental and theoretical studies, it has been possible to understand the crucial role played by the lattice, which can stabilize electronic instabilities and guide the evolution of correlation-driven phenomena such as Mott-Hubbard transitions [1]. However, these studies have concentrated on bulk properties; the surface behavior is rarely discussed and is indeed a more complicated problem. At the surface, the atomic coordination number and screening change, which has an effect on electronic correlations [2], but other factors such as surface reconstruction and lattice defects can also affect the MIT.

Cr-doped  $V_2O_3$  is the prototype Mott-Hubbard material [3–5], presenting a correlation-induced MIT without symmetry breaking. Strong electronic correlation splits the noninteracting bands into interacting upper and lower Hubbard bands. In the metallic phase a strongly renormalized quasiparticle peak remains at the Fermi level, which is reminiscent of the uncorrelated band structure. The phase diagram of  $V_2O_3$  consists of three phases: the paramagnetic insulator (PI), paramagnetic metal (PM), and antiferromagnetic insulator (AFI) [3] phases [see Fig. 1(a)]. The Mott transition takes place between the PI and PM phases; it can be induced by increasing pressure starting from the PI phase, as well as by decreasing temperature for doping levels with a concentration of around 1.1% Cr. The orbital degrees of freedom in  $V_2O_3$  have to be taken into account in order to understand the MIT: the low-lying orbitals are the  $t_{2g}$  orbitals made up of singly degenerate  $a_{1g}$  and doubly degenerate  $e_g$  orbitals in the crystal field of the corundum lattice structure. At the MIT, the  $a_{1g}$  bands are shifted up in energy and the  $e_g$  bands split into two Hubbard bands, with

the Hund's exchange leading to a local spin alignment throughout the transition [6–9]. Although the surface of  $V_2O_3$  has been well studied for the pure compound [10,11], and extensive experimental [12] and theoretical investigations [13] have been carried out on the surface termination of  $V_2O_3$ , very little is known about the effects of the surface on the Mott transition. In this Letter, we explore specific surface effects on the evolution of the Mott transition in  $(V_{1-x}Cr_x)_2O_3$  both experimentally, using x-ray diffraction (XRD) and scanning photoelectron microscopy (SPEM), and theoretically, by density-functional theory plus dynamical mean-field theory (DFT + DMFT) [14–16].

The Mott transition is a first-order transition; therefore, domain coexistence can occur and a large hysteresis is possible. Figure 1(b) shows XRD measurements on a monocrystal done during the temperature-driven phase transition [17]. A large hysteresis is seen, comparable to earlier results [4]. However, at 244 K the transition happens in less than 2 K, whereas in powder XRD the transition lasts 60 K. The major difference between a monocrystal and a powder is the surface-to-bulk ratio. The MIT at the surface might be greatly affected by defects or surface reconstruction. In order to understand this discrepancy, we probe the surface using SPEM.

*Method: Experimental.*—SPEM experiments were performed as a function of temperature on the Escamicroscopy beam line at the Elettra synchrotron, using photons of 400 eV [33]. SPEM uses a direct approach to photoelectron spectromicroscopy; specifically, a focused photon beam, down to 150 nm in diameter, is used to illuminate the sample. Photoelectrons are collected with a hemispherical electron analyzer and detected by a 48-channel electron detector. SPEM can operate in two modes: (i) XPS spectroscopy from a submicron spot or (ii) imaging, where the

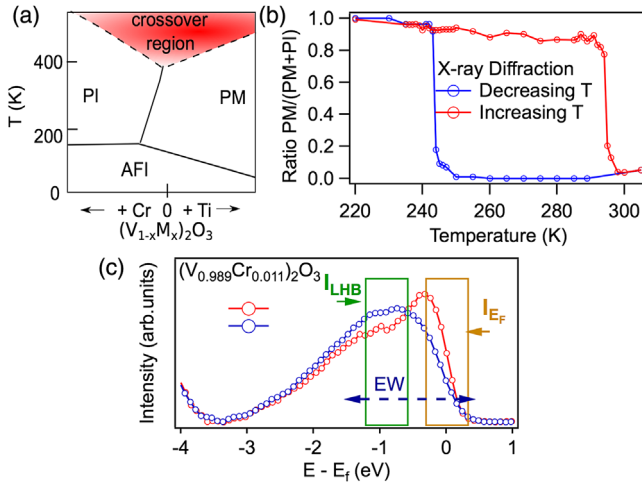


FIG. 1 (color online). (a) Phase diagram for  $(V_{1-x}Cr_x)_2O_3$ . (b) Ratio  $PM/(PM + PI)$  versus temperature probed by x-ray diffraction on a single crystal. (c) Photoemission spectra for  $(V_{1-x}Cr_x)_2O_3$  at  $x = 0.011$ , 300 K, and 200 K, cleaved along the (001) plane. The increase of spectral weight near the Fermi level indicates the phase transition from insulator to metal when decreasing the temperature. The blue arrow shows the energy window (EW) chosen to record the images.  $I_{E_F}$  and  $I_{LHB}$  represent, respectively, the intensity near  $E_F$  and of the lower Hubbard band (LHB). The ratio between the two provides a measure for the metallicity of the probed surface.

sample surface is mapped within a selected kinetic energy. In the imaging mode, all 48 channels are recorded for every pixel of the image. In our experiments a 2-eV energy window near the Fermi level was chosen to observe the MIT, as shown in Fig. 1(c).

As has already been shown in previous SPEM measurements [34], coexisting PM and PI phases in  $(V_{1-x}Cr_x)_2O_3$  can be unambiguously distinguished by the photoemission signal from the outer valence electronic states; this was not attributed to Cr-doping inhomogeneity [35], and the physical origin remained mysterious. With the present study we are able to solve this puzzle. The improved experimental conditions allow us to show a clear correlation between the shape and position of domains at the metal-insulator transition, and the fact that surface structural defects actually favor the formation of metallic domains. This was possible thanks to (i) the use of higher-energy photons, which make it possible to have a clearer spectroscopic contrast on the quasiparticle peak [36], (ii) an improved spatial resolution (150 nm), and (iii) a direct comparative study between different surfaces of the same material. In particular, high-quality single crystals from Purdue University were cleaved in either the (001) or the (102) plane, keeping the [001] direction always pointing towards the electron analyzer that was shown to give the strongest quasiparticle peak in the photoemission signal [37] (see Fig. 2, top). The samples were cleaved and measured under UHV conditions ( $2 \times 10^{-10}$  mbar or better) to avoid surface contamination (the carbon photoemission peak was

regularly checked in the course of the experiment). In order to obtain genuine two-dimensional maps of the PM versus PI concentration at the surface, the photoemission images were corrected for topographic effects [38]. As a measure for the metallicity of the sample, we take the ratio between the intensity near  $E_F$  ( $I_{E_F}$ ) and near the LHB ( $I_{LHB}$ ), see Fig. 1 [39]. For example, in Fig. 1(c) the ratio is 1 in the PM phase and 0.45 in the PI phase. However, with a sample cleaved along the (102) direction, the quasiparticle is less intense; therefore, the ratio in the PM phase is only 0.8 (see Supplemental Material [18] and [2,37]). The images

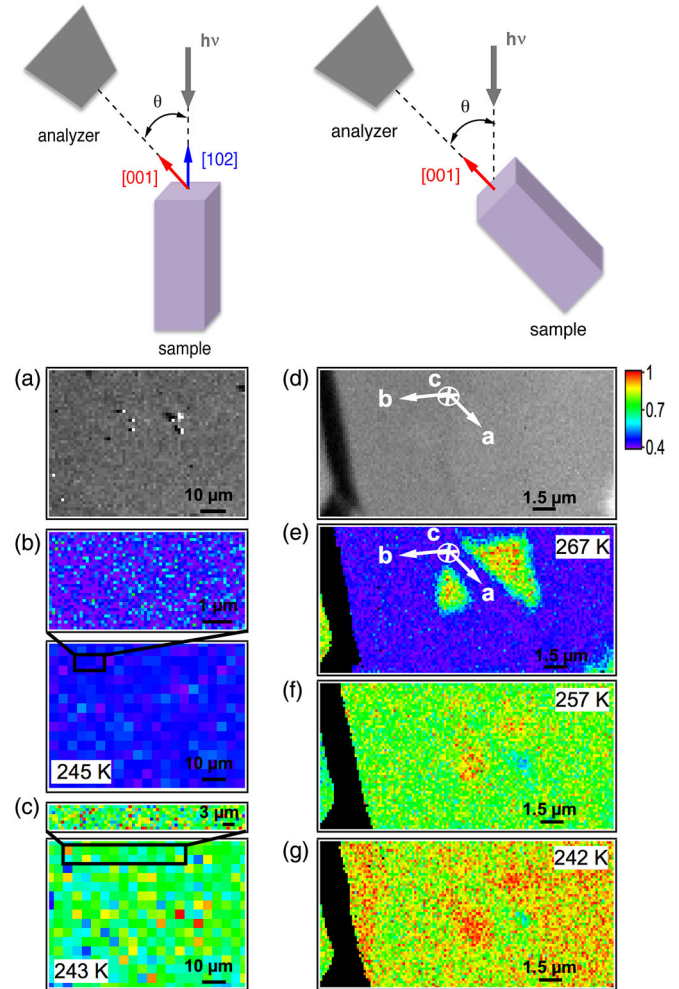


FIG. 2 (color online). Top: Sample orientation versus incoming photons and analyzer. Left: Sample cleaved along the (102) direction with the analyzer in the (001) direction. (a) Surface morphology image taken at a photoelectron energy corresponding to the  $V3p$  core level, and at temperature  $T = 245$  K. (b) Contrast  $I_{E_F}/I_{LHB}$  between the PM and PI phases for 245 K and (c) for 243 K. No coexisting domains could be detected during the phase transition. Right: Sample fractured along the (001) direction with the analyzer in the (001) direction. (d) Surface morphology image. The following images show the contrast between the PM and PI phases at (e)  $T = 267$  K, (f)  $T = 257$  K, and (g)  $T = 242$  K (black pixels are where the ratio is ill defined [39]).

obtained in this way are real-space “metallicity maps” of the sample surface [34].

*SPEM results.*—The left panel of Fig. 2 shows a region on the (102)-cleaved surface at different temperatures while the sample is cooled down. Since the (102) plane is the natural cleaving direction, it can produce large flat surfaces with few defects. In particular, the probed region does not present any significant defects detectable with our spatial resolution (150 nm): this is evident from Fig. 2(a), where the image has not been corrected for surface morphology and which cannot reveal the presence of any topographic defect at the surface. By observing the metallicity images, we found that no MIT could be seen until 245 K [Fig. 2(b)], while the whole surface turned metallic at 243 K [Fig. 2(c)]. This indicates that the transition was too sudden for our experimental conditions to detect the presence of domains, the limiting factor being the relatively long acquisition time for each photoemission image and/or the size of the domains. Hence, we can conclude that, within the limits of our spatial resolution, the entire probed region turns metallic in less than 2 K, similar to the bulk probed by our XRD experiment. Therefore the (102) plane behaves like the bulk material.

On the contrary, when cleaving along the (001) direction, we find coexisting domains on the surfaces over a wide temperature range, starting as soon as 267 K. We start by analyzing an area where no structural defects could be detected with our spatial resolution, as revealed by the uncorrected image in Fig. 2(d). The first metallic domains appear starting at 267 K [Fig. 2(e)]; they present a triangular shape, revealing a clear correlation with the hexagonal symmetry of the (001) plane (the  $a$  and  $b$  crystallographic directions are shown to allow a direct comparison). This strongly suggests that the borders of the metallic domain correspond to surface steps. The rest of the area is still insulating and starts its transformation around 257 K [Fig. 2(f)]. Eventually, at 242 K [Fig. 2(g)], the transition is almost complete, similar to the (102) plane. On the (001) surface, the sample also has regions with significant amounts of large defects; several black lines (cracks) are visible in the morphology image. In this highly defected region, large metallic domains appear. Let us now focus our analysis on smaller defects, which are less pronounced in Fig. 3 but more easy to understand. These smaller defects most likely correspond to cleavage steps, such as the one found in the  $S$  area shown in detail in Fig. 3(c): the metallic domains appear to follow the cleavage step direction (see the morphology image in Supplemental Material [18]). Overall, metallic domains are present for the (001) surface well above 243 K, the transition temperature of the (102) plane.

Our experimental findings confirm that structural defects can act as nucleating centers for the insulator-to-metal transition, thus guiding the evolution of the formation of domains during the phase coexistence [34]. Surprisingly, they also clearly indicate that structural defects at the

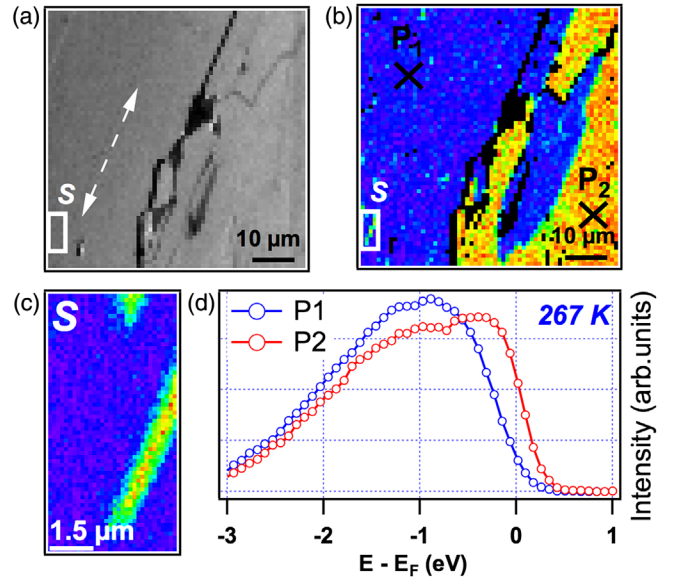


FIG. 3 (color online). Sample cut along the (001) plane at 267 K. (a) Surface morphology image with a crack in the middle and a cleavage step marked by the dashed arrow; the  $S$  box is at its extremity. (b) The corresponding phase-contrast images show the apparition of metallic domains starting at 267 K. The large domains are separated by cracks in the sample. (c) Close-up image of a cleavage step, which presents a more metallic behavior. (d) Photoemission spectra from the  $P_1$  and  $P_2$  points.

surface of  $(V_{1-x}Cr_x)_2O_3$  favor the formation of a metallic phase over an insulating one.

*Theory.*—One might envisage the cleavage steps as an extra surface, and that surface effects should, thus, be enhanced. However, the usual suspects of electronic correlations at (enhanced) surfaces, i.e., an enhanced  $U$  because of the reduced screening and the removed hopping perpendicular to the surface, suggest the surface and cleavage steps to be more insulating. We find the contrary: they are more metallic.

As these simple explanations fail, we need to inspect the surface more thoroughly, including the proper surface reconstruction. DFT calculations [40] indicate, depending on the oxygen partial pressure, a VO surface termination with various excesses of vanadyl or a  $O_3$  termination. The former has also been identified in some experiments [11–13,41,42]. Figure 4 shows the actual supercells with VO and  $O_3$  terminations that we consider in our calculation. One can envisage the surface as consisting of several layers of the stoichiometric  $(V-O_3-V)$  unit cell, i.e.,  $(V-O_3-V)(V-O_3-V)\dots(V-O_3-V)$  plus an extra V or  $(O_3-V)$  layer for the VO and  $O_3$  termination, respectively; see Fig. 4 (upper panel).

*Method: Theory.*—We perform a full relaxation of the VO- and  $O_3$ -terminated  $V_2O_3$  surfaces in the corundum structure, including a 12-Å-thick vacuum layer, using the Vienna *ab initio* simulation package (VASP) [43,44], with a GGA-PBE functional [45]. In the case of the  $O_3$  termination, the large polarity of the surface is compensated by a

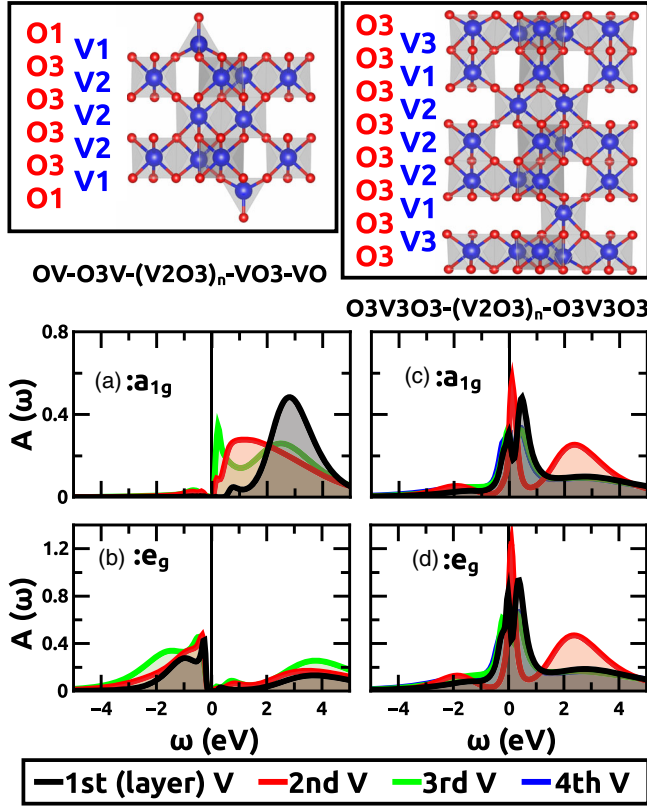


FIG. 4 (color online). Top: VO termination (left) and O<sub>3</sub> termination (right) supercell. Below the figures, we indicate how the supercell is made up from the stoichiometric (V-O<sub>3</sub>-V) supercell plus the surface termination. For the O<sub>3</sub> termination, one V moves from the second to the first layer because of the surface reconstruction. Bottom: Layer- and orbital-resolved spectral function  $A(\omega)$  for the VO termination [(a)–(b)] and for the (O<sub>3</sub>) termination [(c)–(d)]. The more excess oxygen at the surface, the more metallic are the surface layers.

surface reconstruction where one subsurface V atom moves from the second layer to the first (surface) layer, so that (O<sub>3</sub>-V)(V-O<sub>3</sub>-V)(V-O<sub>3</sub>-V)... actually becomes (O<sub>3</sub>-V<sub>3</sub>-O<sub>3</sub>)(V-O<sub>3</sub>-V)... The surface reconstruction for the VO termination is less dramatic.

After atomic relaxation, we project the corresponding Wien2K [46] band structure onto Wannier functions using Wien2Wannier [32,47] and supplement it by a local Kanamori interaction with intraorbital  $U=5.5$  eV, interorbital  $U'=4.1$  eV and Hund's exchange  $J=0.7$  eV. The interaction parameters are taken a bit larger than in the literature [6–8,48]; this is done because of the reduced screening at the surface and also to account for the more insulating nature at the experimental 1.1% Cr doping, which is too small to take into account in the supercell of our calculations. The resulting Hamiltonian is then solved by DMFT at room temperature, 300 K, using continuous-time quantum Monte Carlo simulations in the hybridization expansions [49] (w2dynamic code [50]) and the maximum entropy method [51] for an analytic continuation of the spectra.

**DFT + DMFT results.**—Figure 4 (lower panels) shows the DFT + DMFT spectra for VO (left) and O<sub>3</sub> termination (right), resolved for the  $a_{1g}$  and  $e_g^\pi$  orbitals and the different layers. The VO-terminated surface is insulating at this interaction strength and temperature. Compared to a  $3d^2$  electronic configuration for all V atoms, the vanadyl termination adds 1 extra O to each (V-O<sub>3</sub>-V) unit cell in the layer, i.e., 1 hole per V in the layers. According to our DFT + DMFT results, this hole is, however, bound to the surface layer (where the single V in the surface layer is in a V<sup>4+</sup> or  $3d^1$  configuration) and to the second layer (where one of the two V atoms is V<sup>4+</sup>). The other V atom in the second layer and all other V in the further subsurface layers are in a V<sup>4+</sup> or  $3d^2$  configuration. This charge disproportionation explains why, despite the doping, the surface may remain insulating. (Note that Fig. 4 show the layer-averaged spectrum; the Supplemental Material [18] it is resolved for the two inequivalent sites of the second layer.) If we reduce the interaction strength, the VO-terminated surface becomes metallic. Indeed, the VO terminated surface is more metallic than bulk V<sub>2</sub>O<sub>3</sub>; i.e., it stays metallic up to larger values of the Coulomb interaction (see Supplemental Material [18]).

On the other hand, the O<sub>3</sub> termination (Fig. 4, right) is already metallic at the same Coulomb interaction and temperature. The most metallic layer is the surface layer, and the width of the central quasiparticle peak shrinks from layer to layer. The fourth, central layer is already close to the bulk result (see Supplemental Material [18]). The reason why the surface layer is more metallic, despite the reduced hopping, is the even larger hole doping due to the O<sub>3</sub> termination. In the case of the O<sub>3</sub> termination, the (O<sub>3</sub>-V<sub>2</sub>) slab adds to the stoichiometric (V-O<sub>3</sub>-V) layers 3 holes per (V-O<sub>3</sub>-V) unit cell in the layers (or 1.5 holes per V atom). These 1.5 holes are now, however, distributed to 3 surface layers in the DFT + DMFT charge distribution: 1.2 electrons per V for the first layer, 1.5 per V for the second layer, 1.9 per V for the third layer, and 2.00 (i.e., the bulk value) for the fourth layer. That is, for the O<sub>3</sub> termination, vanadium is neither V<sup>4+</sup> nor V<sup>3+</sup> but in between. Consequently, the system is more itinerant, and the (001) surface layers of V<sub>2</sub>O<sub>3</sub> are metallic. Let us emphasize that the extra oxygen stabilizes the polar (001) surface. This is not the case for the (102) layer, which is thus more stable stoichiometrically and more insulating (see Supplemental Material [18]).

We can, hence, conclude that excess oxygen makes the (reconstructed) surface more metallic due to hole doping. The additional surface at the steps indicates an extra surface doping such that V<sub>2</sub>O<sub>3</sub> will be even more metallic at such edges. This is akin to our description of the O<sub>3</sub> termination versus the VO termination. As we have seen, this larger amount of doping does not have a very big effect, but it shifts the critical Coulomb interaction for the Mott-Hubbard transition somewhere to the left of the phase diagram (Fig. 1, inset). That means the transition temperature increases, as we found experimentally. It also explains

our experiment in Fig. 3; the cleave step is more metallic because of an accumulation of excess oxygen at the corner.

*Conclusions.*—We observed experimentally that at the PI-PM Mott transition in  $(V_{1-x}Cr_x)_2O_3$ , metallic domains appear at higher temperatures than at the bulk transition. Their evolution is determined by the surface crystallographic direction and along the cleaving steps. Our DFT + DMFT theoretical calculations show that a surface reconstruction with an excess of oxygen favors the formation of a metallic phase. Against common wisdom, surfaces can hence be more metallic than the bulk, and surface steps even more so. This effect observed here for  $(V_{1-x}Cr_x)_2O_3$  can be of general interest for surfaces of strongly correlated oxides, oxide heterostructures, and nanostructure.

L. S. and K. H. acknowledge financial support by European Research Council under the European Union's Seventh Framework Program (FP/2007-2013)/ERC through Grant No. 306447 and the Doctoral School W1243 Solids4Fun by the Austrian Science Fund (FWF). Calculations have been done on the Vienna Scientific Cluster (VSC). G. L., M. H., E. P., and M. M. acknowledge financial support by the EU/FP7 under the contract Go Fast (Grant No. 280555) and by "Investissement d'Avenir Labex PALM (Grant No. ANR-10-LABX-0039-PALM). The SPEM experiments have received funding from the European Community's Seventh Framework Program (FP7, Grant No. 312284).

\*Present address: Institute for Quantum Electronics, Physics Department, ETH Zurich, CH-8093 Zurich, Switzerland. gabriel.lantz88@gmail.com

- [1] M. Imada, A. Fujimori, and Y. Tokura, *Rev. Mod. Phys.* **70**, 1039 (1998).
- [2] G. Borghi, M. Fabrizio, and E. Tosatti, *Phys. Rev. Lett.* **102**, 066806 (2009).
- [3] D. B. McWhan, T. M. Rice, and J. P. Remeika, *Phys. Rev. Lett.* **23**, 1384 (1969).
- [4] D. B. McWhan and J. P. Remeika, *Phys. Rev. B* **2**, 3734 (1970).
- [5] P. Hansmann, A. Toschi, G. Sangiovanni, T. Saha-Dasgupta, S. Lupi, M. Marsi, and K. Held, *Phys. Status Solidi (b)* **250**, 1251 (2013).
- [6] K. Held, G. Keller, V. Eyert, D. Vollhardt, and V. I. Anisimov, *Phys. Rev. Lett.* **86**, 5345 (2001).
- [7] G. Keller, K. Held, V. Eyert, D. Vollhardt, and V. I. Anisimov, *Phys. Rev. B* **70**, 205116 (2004).
- [8] A. I. Poteryaev, J. M. Tomczak, S. Biermann, A. Georges, A. I. Lichtenstein, A. N. Rubtsov, T. Saha-Dasgupta, and O. K. Andersen, *Phys. Rev. B* **76**, 085127 (2007).
- [9] J. H. Park, L. H. Tjeng, A. Tanaka, J. W. Allen, C. T. Chen, P. Metcalf, J. M. Honig, F. M. F. de Groot, and G. A. Sawatzky, *Phys. Rev. B* **61**, 11506 (2000).
- [10] A. J. Window, A. Hentz, D. C. Sheppard, G. S. Parkinson, H. Niehus, D. Ahlbrecht, T. C. Q. Noakes, P. Bailey, and D. P. Woodruff, *Phys. Rev. Lett.* **107**, 016105 (2011).
- [11] F. E. Feiten, J. Seifert, J. Paier, H. Kühlenbeck, H. Winter, J. Sauer, and H. J. Freund, *Phys. Rev. Lett.* **114**, 216101 (2015).
- [12] S. Surnev, M. Ramsey, and F. Netzer, *Prog. Surf. Sci.* **73**, 117 (2003).
- [13] C. Kolczewski, K. Hermann, S. Guimond, H. Kühlenbeck, and H. J. Freund, *Surf. Sci.* **601**, 5394 (2007).
- [14] V. I. Anisimov, A. I. Poteryaev, M. A. Korotin, A. O. Anokhin, and G. Kotliar, *J. Phys. Condens. Matter* **9**, 7359 (1997); A. I. Lichtenstein and M. I. Katsnelson, *Phys. Rev. B* **57**, 6884 (1998).
- [15] G. Kotliar, S. Y. Savrasov, K. Haule, V. S. Oudovenko, O. Parcollet, and C. A. Marianetti, *Rev. Mod. Phys.* **78**, 865 (2006).
- [16] K. Held, I. A. Nekrasov, G. Keller, V. Eyert, N. Blümer, A. McMahan, R. Scalettar, T. Pruschke, V. I. Anisimov, and D. Vollhardt, *Phys. Status Solidi (b)* **243**, 2599 (2006); K. Held, *Adv. Phys.* **56**, 829 (2007).
- [17] More details on the XRD measurements can be found in the Supplemental Material [18].
- [18] See Supplemental Material at <http://link.aps.org/supplemental/10.1103/PhysRevLett.115.236802> for x-ray diffraction, temperature calibration, DFT and DMFT computational details and (102) surface termination, which includes Refs. [19–23,24–32].
- [19] A. L. Tiano, J.-B. Li, E. Sutter, S. S. Wong, and M.-V. Fernandez-Serra, *Phys. Rev. B* **86**, 125135 (2012).
- [20] W. R. Robinson, *Acta Crystallogr. Sect. B* **31**, 1153 (1975).
- [21] I. S. Elfimov, T. Saha-Dasgupta, and M. A. Korotin, *Phys. Rev. B* **68**, 113105 (2003).
- [22] F. Pfuner, J. Schoiswohl, M. Sock, S. Surnev, M. Ramsey, and F. Netzer, *J. Phys. Condens. Matter* **17**, 4035 (2005).
- [23] Q. Luo, Q. Guo, and E. Wang, *Appl. Phys. Lett.* **84**, 2337 (2004).
- [24] M. Potthoff and W. Nolting, *Phys. Rev. B* **60**, 7834 (1999).
- [25] J. K. Freericks, *Transport in Multilayered Nanostructures: The Dynamical Mean-Field Theory Approach* (Imperial College Press, London, 2006).
- [26] H. N. Waltenburg and J. T. Yates, *Chem. Rev.* **95**, 1589 (1995); J. Dabrowski and H.-J. Müssig, *Silicon Surfaces and Formation of Interfaces: Basic Science in the Industrial World* (World Scientific, Singapore, 2000).
- [27] U. Diebold, *Surf. Sci. Rep.* **48**, 53 (2003).
- [28] P. Hansmann, T. Ayril, L. Vaugier, P. Werner, and S. Biermann, *Phys. Rev. Lett.* **110**, 166401 (2013); *J. Phys. Condens. Matter* **25**, 094005 (2013).
- [29] T. Eelbo, M. Wasniowska, P. Thakur, M. Gyamfi, B. Sachs, T. O. Wehling, S. Forti, U. Starke, C. Tieg, A. I. Lichtenstein, and R. Wiesendanger, *Phys. Rev. Lett.* **110**, 136804 (2013).
- [30] I. Di Marco, J. Minar, S. Chadov, M. I. Katsnelson, H. Ebert, and A. I. Lichtenstein, *Phys. Rev. B* **79**, 115111 (2009).
- [31] S. Gardonio, M. Karolak, T. O. Wehling, L. Petaccia, S. Lizzit, A. Goldoni, A. I. Lichtenstein, and C. Carbone, *Phys. Rev. Lett.* **110**, 186404 (2013).
- [32] J. Kunes, R. Arita, P. Wissgott, A. Toschi, H. Ikeda, and K. Held, *Comput. Phys. Commun.* **181**, 1888 (2010).
- [33] M. K. Abyaneh, L. Gregoratti, M. Amati, M. Dalmiglio, and M. Kiskinova, *e-J. Surf. Sci. Nanotechnol.* **9**, 158 (2011).
- [34] S. Lupi *et al.*, *Nat. Commun.* **1**, 105 (2010).
- [35] D. D. Sarma, D. Topwal, U. Manju, S. R. Krishnakumar, M. Bertolo, S. La Rosa, G. Cautero, T. Y. Koo, P. A. Sharma,

- S.-W. Cheong, and A. Fujimori, *Phys. Rev. Lett.* **93**, 097202 (2004).
- [36] S.-K. Mo, J. D. Denlinger, H.-D. Kim, J.-H. Park, J. W. Allen, A. Sekiyama, A. Yamasaki, K. Kadono, S. Suga, Y. Saitoh, T. Muro, P. Metcalf, G. Keller, K. Held, V. Eyert, V. I. Anisimov, and D. Vollhardt, *Phys. Rev. Lett.* **90**, 186403 (2003).
- [37] F. Rodolakis, B. Mansart, E. Papalazarou, S. Gorovikov, P. Vilmercati, L. Petaccia, A. Goldoni, J. P. Rueff, S. Lupi, P. Metcalf, and M. Marsi, *Phys. Rev. Lett.* **102**, 066805 (2009).
- [38] M. Marsi, L. Casalis, L. Gregoratti, S. Gunther, A. Kolmakov, J. Kovac, D. Lanza, and M. Kiskinova, *J. Electron Spectrosc. Relat. Phenom.* **84**, 73 (1997).
- [39] Pixels from highly defected regions, where the ratio is ill defined, are left black in the figures.
- [40] G. Kresse, S. Surnev, J. Schoiswohl, and F. P. Netzer, *Surf. Sci.* **555**, 118 (2004).
- [41] A. C. Dupuis, M. Abu Haija, B. Richter, H. Kuhlenbeck, and H. J. Freund, *Surf. Sci.* **539**, 99 (2003).
- [42] J. Schoiswohl, M. Sock, S. Surnev, M. G. Ramsey, F. P. Netzer, G. Kresse, and J. N. Andersen, *Surf. Sci.* **555**, 101 (2004).
- [43] G. Kresse and J. Hafner, *Phys. Rev. B* **48**, 13115 (1993).
- [44] G. Kresse and J. Furthmüller, *Comput. Mater. Sci.* **6**, 15 (1996).
- [45] J. P. Perdew, K. Burke, and M. Ernzerhof, *Phys. Rev. Lett.* **77**, 3865 (1996).
- [46] P. Blaha, K. Schwarz, G. Madsen, D. Kvasnicka, and J. Luitz, *An Augmented Plane Wave+Local Orbitals Program for Calculating Crystal Properties* (Vienna University of Technology, Vienna, 2001).
- [47] A. A. Mostofi, J. R. Yates, Y.-S. Lee, I. Souza, D. Vanderbilt, and N. Marzari, *Comput. Phys. Commun.* **178**, 685 (2008).
- [48] J. M. Tomczak and S. Biermann, *Phys. Rev. B* **80**, 085117 (2009).
- [49] E. Gull, A. J. Millis, A. I. Lichtenstein, A. N. Rubtsov, M. Troyer, and P. Werner, *Rev. Mod. Phys.* **83**, 349 (2011).
- [50] N. Parragh, A. Toschi, K. Held, and G. Sangiovanni, *Phys. Rev. B* **86**, 155158 (2012).
- [51] J. E. Gubernatis, M. Jarrell, R. N. Silver, and D. S. Sivia, *Phys. Rev. B* **44**, 6011 (1991); A. W. Sandvik, *Phys. Rev. B* **57**, 10287 (1998).